PNAS RESEARCH ARTICLE | EARTH, ATMOSPHERIC, AND PLANETARY SCIENCES

Modeling energy requirements for oxygen production on the Moon

Dorian Leger[a,b,1], Fardin Ghaffari-Tabrizi[a], Matthew Shaw[c], Joshua Rasera[d], David Dickson[e], Baptiste Valentin[f,g], Anton Morlock[h], Freja Thoresen[a], and Aidan Cowley[a,1]

Affiliations are included on p. 10.

Edited by Alexis Bell, University of California, Berkeley, CA; received April 19, 2023; accepted October 28, 2024

Spacecraft using combustion engines require substantial amounts of oxygen for their propellant. The Moon could be a source of oxygen for rocket propellant, since the material composing the lunar surface can be processed to extract oxygen. However, little is known about overall energy requirements of the processes described in the literature for oxygen extraction from lunar regolith. This knowledge gap constrains the planning of lunar missions, since the scale of energy infrastructure required for oxygen production facilities is not well characterized. This study presents an energy consumption model for oxygen production via hydrogen reduction of the mineral ilmenite ($FeTiO_3$). We consider an end-to-end production chain starting from dry regolith as the feedstock. The production includes the following process steps: excavation, transportation, beneficiation, hydrogen reduction, water electrolysis, liquefaction, and zero boil-off storage. The model predicts the energy demand per kilogram oxygen produced based on adjustable parameters for each process step. As expected, the model indicates a strong dependence on feedstock composition. For regolith composed of 10 wt% ilmenite, the model predicts that a total of 24.3 (± 5.8) kWh is needed per kg of liquid oxygen produced. This study confirms that the hydrogen reduction and electrolysis steps have the highest energy requirements in the production chain. Sensitivity analysis reveals that the enrichment factor of the beneficiation process is the most critical parameter for optimizing energy utilization. Overall, this study provides a parameterized end-to-end model of energy consumption that can serve as a foundation for various production systems on the Moon.

lunar oxygen production | energy requirements | hydrogen reduction process | in-situ resource utilization | space exploration

Significance

Oxygen plays a crucial role in the growing space economy as an oxidizer for rocket propellants and human life support. Studies predict that sourcing oxygen from the Moon's raw materials can improve space transport architecture due to its shallower gravity well, and can support permanent settlements in the Solar System. However, there are currently no dedicated models for the energy requirements of oxygen production on the Moon that consider entire production chains. This study provides an energy analysis from raw material to stored liquid oxygen for a promising lunar oxygen production technology, which can assist in comparing technologies, and provides data for techno-economic assessments. Our findings have significant implications for optimizing locations of future lunar oxygen production sites.

Driven by significant efforts from both space agencies and private enterprises, there is a rapidly growing momentum toward establishing permanent settlements on the Moon and Mars in this century (1). As humanity expands into the Solar System, in situ resource utilization (ISRU) is needed to ensure critical supply chains (2, 3). Oxygen is a fundamental commodity needed for the space economy due to its role in life-support systems (4), and as an oxidizer in the propellant of spacecraft and satellites (5–7). Oxygen comprises approximately 80% or more of the mass for most combustion based propellants, such as methalox and hydrolox rockets (8, 9). In order to lift or land cargo from a planetary body with a mass greater than a small asteroid (~10^7 to ~10^8 Gtonnes) (10, 11), chemical rockets are required (12–14), which commonly use oxygen as the oxidizing agent (13). Producing oxygen on the Moon instead of on Earth can be economically advantageous due to the Moon's weaker gravity (8). Hence, less propellant is needed to launch cargo into orbit from the lunar surface compared to launches from Earth's surface (8). If Earth-based rockets could refuel in space, for example at a propellant depot placed in Earth-Moon Lagrange point 1 (EML1) this could greatly improve the launch efficiency (8). As a rule of thumb, rockets launched from Earth destined for EML1 must burn ~25 kg of propellant to transport 1 kg of payload, whereas rockets launched from the Moon to EML1 would burn only ~4 kg of propellant to transport 1 kg of payload (15). The development of a cislunar refueling station supported by lunar resources is now viewed as a key stepping stone toward permanent settlements in the Solar System (6, 16–18). In the future, asteroid mining may also supply oxygen for the space economy (19); however, this study focuses on lunar-derived oxygen.

The lunar surface is covered by an unconsolidated layer of material called regolith that is made of several meters of rocks, fine-grained material, and glass particles (20). Geographically, the Moon has two distinct features called Highland and Mare which differ in regolith properties (21). The Mare regions appear darker and are rich in iron, while the so-called High-Ti Mare are also rich in titanium. The Highland regions appear lighter

Author contributions: D.L. and A.C. designed research; D.L., F.G.-T., M.S., D.D., and B.V. performed research; D.L., F.G.-T., M.S., J.R., D.D., B.V., A.M., and F.T. contributed new reagents/analytic tools; D.L., F.G.-T., J.R., D.D., B.V., and A.C. analyzed data; D.L., M.S., J.R., and A.C. critical review; D.L., F.G-T., and A.M. data visualization; and D.L., M.S., and J.R. wrote the paper.

Competing interest statement: D.L. is CEO and cofounder of Cx Bio.

This article is a PNAS Direct Submission.

[1]To whom correspondence may be addressed. Email: dorian.leger@cxbio.io or aidan.cowley@esa.int.

This article contains supporting information online at https://www.pnas.org/lookup/suppl/doi:10.1073/pnas.2306146122/-/DCSupplemental.

Published February 18, 2025.

and are rich in aluminum silicates, specifically anorthite ($CaAl_2Si_2O_8$). Regolith thickness varies between 4 to 5 m and 10 to 15 m in Mare and Highland regions respectively (22). The element oxygen comprises approximately 45% by mass of the lunar regolith, but is mostly bound in strong chemical bonds to other elements (23). The oxide abundances in regolith samples from Mare and Highland recovered by Luna and Apollo missions showed variability and were approximately SiO_2 (45 wt%), followed by Al_2O_3 (11 to 20 wt%), FeO (5 to 20 wt%), CaO (11 to 17 wt%), MgO (4 to 10 wt%), TiO_2 (0.5 to 8 wt%) (20). Of these oxide components, iron oxides are more easily reduced to liberate the oxygen (*SI Appendix*). Regolith has been created by over 4.5 billion years of asteroid impacts, solar wind, and radiation (24). The regolith contains a fraction of agglutinates, created from the joining of preexisting grains by impact glass formed by meteorite collisions. Lunar regolith is unlike terrestrial material, because it is not subjected to weathering by an atmosphere and water. Mineralogically, the Highlands are primarily composed of lighter minerals like plagioclase, and constitute the majority of the Moon's regolith (25, 26). The Mare regions, originating later from asteroidal impacts and subsurface volcanism, contain heavier minerals like ilmenite, pyroxene, and olivine (25, 26).

Over 20 candidate technologies have been identified for the production of oxygen on the Moon (5, 27, 28). The element oxygen occurs primarily in two forms on the lunar surface: in ubiquitous oxygen-bearing minerals in lunar regolith and in water-ice predicted to be found primarily in permanently shadowed regions, such as craters, at the south pole (29). Oxygen can be extracted from water-ice-containing regolith by heating the regolith, capturing the released water vapor and performing water electrolysis (30). Oxygen can also be produced from nonicy regolith by employing redox reactions, such as hydrogen reduction (31), molten salt electrolysis/FFC (4), molten regolith electrolysis (32), carbothermal reduction (33), ionic liquid processing (34), and vapor phase pyrolysis (22). These technologies enable liberating oxygen from different minerals and require different amounts of power or heat. Furthermore, these technologies have different upstream processing requirements. Since the production chains vary substantially, end-to-end production chain modeling is necessary to quantitatively compare the energy consumption of these technologies. Space agencies have identified the need to improve the understanding of system power requirements for ISRU oxygen production as a Strategic Knowledge Gap, falling under the Lunar Production Efficiency II category of the International Space Exploration Coordination Group ISRU Gap Assessment Report of 2021 (17).

Among the various technologies for lunar oxygen production, reduction of ilmenite ($FeTiO_3$ or $FeOTiO_2$) using hydrogen gas (commonly referred to as hydrogen reduction) is one of the most mature, has the most available data, and is often used as a baseline for comparisons (23, 35–37). Hydrogen reduction of ilmenite for lunar oxygen production was first described in 1979 by William et al. (38, 39), and was granted a now expired patent in 1990 (40). Currently, at least two known prototype systems exist of this technology, ProSPA which may fly on a NASA CLPS mission (41) and a breadboard demo plant called ALCHEMIST-ED located in Luxembourg (42).

The hydrogen reduction process consists of heating beneficiated regolith between 800 to 1100 °C which enables the reaction of hydrogen gas with the FeO in ilmenite to produce Fe, TiO_2, and H_2O ($H_2 + FeOTiO_2 \rightarrow H_2O + Fe + TiO_2$), where water is subsequently condensed and electrolyzed to form molecular oxygen (O_2) and hydrogen (H_2). Modeling this process for oxygen production is simpler than others, because it primarily liberates oxygen that is found in ilmenite, with minimal reactions of hydrogen with other compounds in the regolith. Thus, for the purpose of estimating energy consumption, this enables abstracting from the complex nature of regolith mineralogy without losing substantial accuracy. In other words, the main regolith mineralogical property that must be known to model hydrogen reduction is the ilmenite concentration. Therefore, to develop this end-to-end model, we prioritized the investigation of hydrogen reduction. We made several additional assumptions to reduce the complexity of the model. For example, we assume that the regolith feedstock has sufficient liberation, such that ilmenite and gangue (nonreactive material) can be separated during beneficiation (enrichment), and the particle size is sufficiently small to allow ~50% of the ilmenite in a particle to react. Furthermore, we neglect the impact of contaminants such as hydrogen sulfide (H_2S) or hydrochloric acid (HCl) which could form troilite (FeS) or chlorapatite ($Ca_5(PO_4)_3Cl$), respectively, and require gas clean-up prior to electrolysis (39). We do not account for hydrogen leakage which would primarily impact system mass, nor the indigenous presence of hydrogen in the regolith, estimated to be ~150 ppm (39). We neglect the potential of oxygen leakage in the production chain. Finally, we conservatively neglect the potential for H_2 reduction to liberate oxygen that is found in TiO_2, in glass phase FeO, and in silicate minerals present in the regolith. Our model is agnostic to the potential energy sources such as photovoltaics or nuclear energy.

Although there are existing studies on the energy requirements for oxygen production via hydrogen reduction, these studies mainly focus on the hydrogen reduction step itself with little consideration of the rest of the production chain (27, 43, 44). Other studies consider the entire process chain, but are focused on metals production, hardware mass, and mass payback ratios (45). More information on existing literature for energy requirements for lunar oxygen production is provided in the *Discussion* and Dataset S1G.

This study presents an end-to-end energy consumption model for oxygen production via hydrogen reduction of ilmenite. The model is modular, such that individual processes can be replaced, and individual parameters can be updated with additional data from future lunar exploration. This study aims to quantify the energy required per kg of liquid oxygen produced as a function of ilmenite concentration in the raw regolith material. It compares the energy requirements of the individual process units and identifies the most influential parameters along the production chain. Additionally, a preliminary location-dependent assessment of the energy requirements of oxygen production is performed, which is visually represented on a map of the lunar surface.

Results

The energy required for the end-to-end production of liquid oxygen on the Moon starting from regolith is considered. The process units in the model are displayed in Fig. 1. The energy consumption model calculates the electrical energy required per unit mass of liquid oxygen produced. The analysis is performed in two parts: a mass yield analysis and an energy requirement analysis. The calculations are performed per 1 kg regolith input, and then the results are normalized to 1 kg liquid oxygen output (1 kg LOX). Across the production chain, the energy requirement, mass conversion efficiency, and composition of flows are calculated (*Methods*). The model considers a mineral composition of the regolith ranging from 1 to 15% ilmenite. This model serves as a baseline solved with simplifying assumptions, upon which more complexity can be added in the future. Therefore, this model does

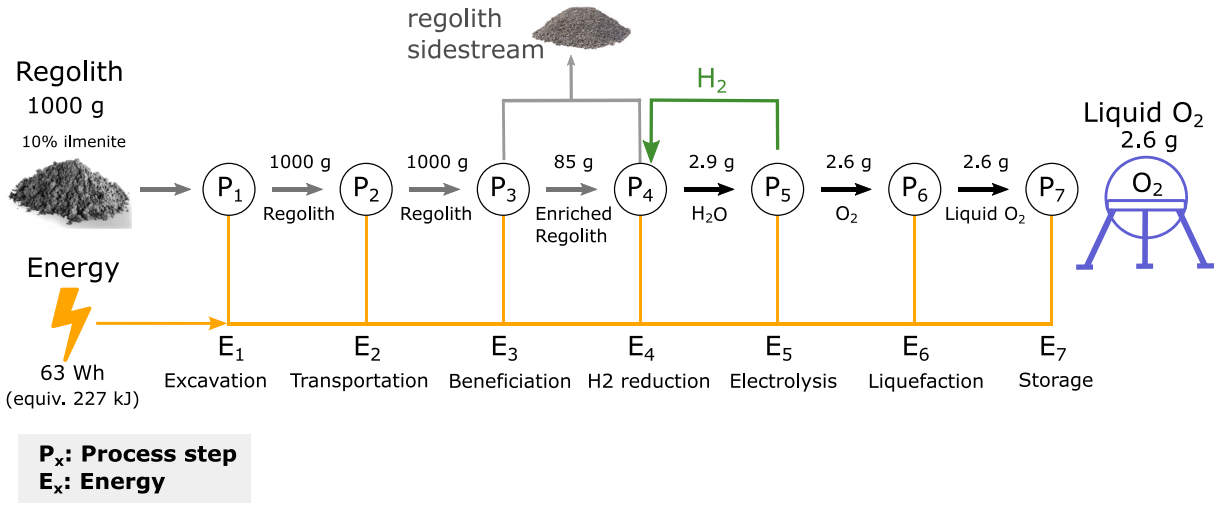

Fig. 1. Regolith to oxygen mass flow and energy requirements diagram. P_1 relates to specialized rovers that excavate regolith from the lunar surface. P_2 corresponds to the transportation of regolith to a processing facility. P_3 refers to the beneficiation system which enriches the concentration of ilmenite ($FeTiO_3$) and rejects unwanted materials. P_4 describes the high-temperature reactor, in which hydrogen (H_2) reacts with the FeO in ilmenite at 900 °C forming Fe and H_2O. Subsequently, gaseous water is removed from the reaction chamber and condensed into liquid water, which is transferred to step P_5, electrolysis. P_5 relates to water being electrochemically split into hydrogen (H_2) and oxygen (O_2). The hydrogen (H_2) is recycled back toward step P_4. P_6 describes the cryocooling step, which converts oxygen from gaseous to liquid state (at −183 °C). Finally, process P_7 describes zero-boil-off storage of liquid oxygen. In the modeling, each process has an input and output substance, and the process may alter the mass and chemical composition of the substance. Furthermore, each process has energy requirements, which are calculated based on empirical data and first principles, as explained in *Methods*.

not consider the impacts of soil maturity, Mg inclusion in TiO_2, nor the impact of particle size. Instead, the model considers only one mineralogical parameter for regolith which is the ilmenite concentration of the feedstock. Furthermore, it is assumed that all ilmenite is in a state that can react with hydrogen, and that ~50% of the ilmenite will react. Since this study uses hydrogen reduction of ilmenite, the energy cost per kg LOX is a function of the ilmenite concentration in the regolith (i.e., the head grade ilmenite).

Fig. 2*A* shows the relative energy consumption across the production chain with respect to variable ilmenite concentration in the regolith (ilmenite wt%). In Fig. 2*B* a specific value of 10 wt% ilmenite is chosen for the baseline results, and the relative energy consumption for each process unit is depicted in more detail. The value of 10 wt% ilmenite is chosen to represent a feedstock with relatively favorable ilmenite concentration, where hydrogen reduction technology is more likely to be suitable. This concentration level could be found, for example, in Mare Tranquillitatis (46). The total energy consumed across the production chain for 10 wt% ilmenite feedstock is 24.3 (±5.8) kWh/kg LOX. As indicated in Fig. 2*B*, the model predicts that the largest electricity consumers are hydrogen reduction (~55%), electrolysis (~38%), and liquefaction (~4.8%). The energy consumption of excavation, transportation, beneficiation, and storage is much lower, with a combined consumption of less than 5%. Notably, the energy required per kg LOX for electrolysis, liquefaction, and storage does not change with ilmenite concentration. On the other hand, the energy per kg LOX consumed by the hydrogen reduction step

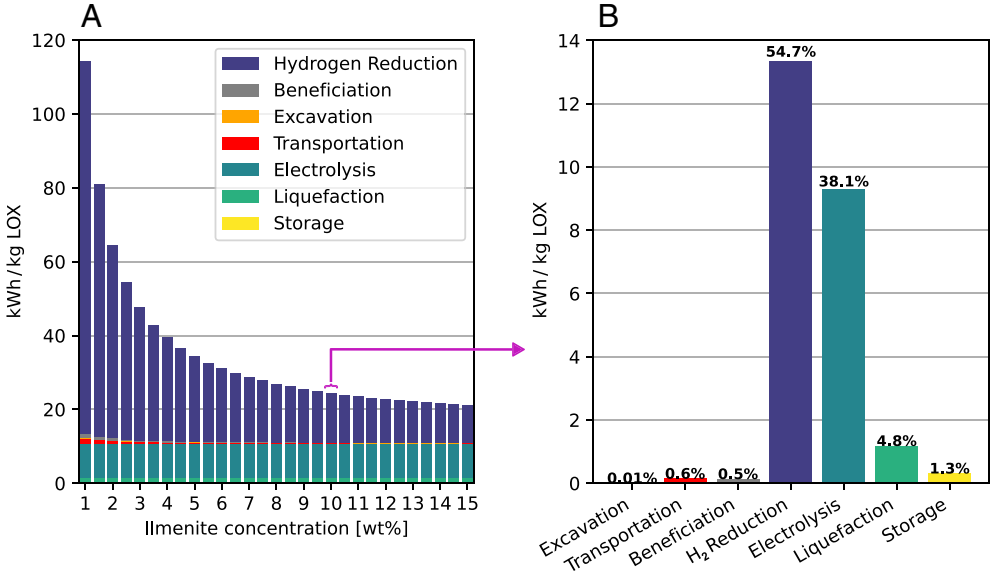

Fig. 2. Predicted utilization of energy per kg LOX across the regolith-to-oxygen production chain, (*A*) as a function of ilmenite concentration and (*B*) at 10 wt% ilmenite concentration.

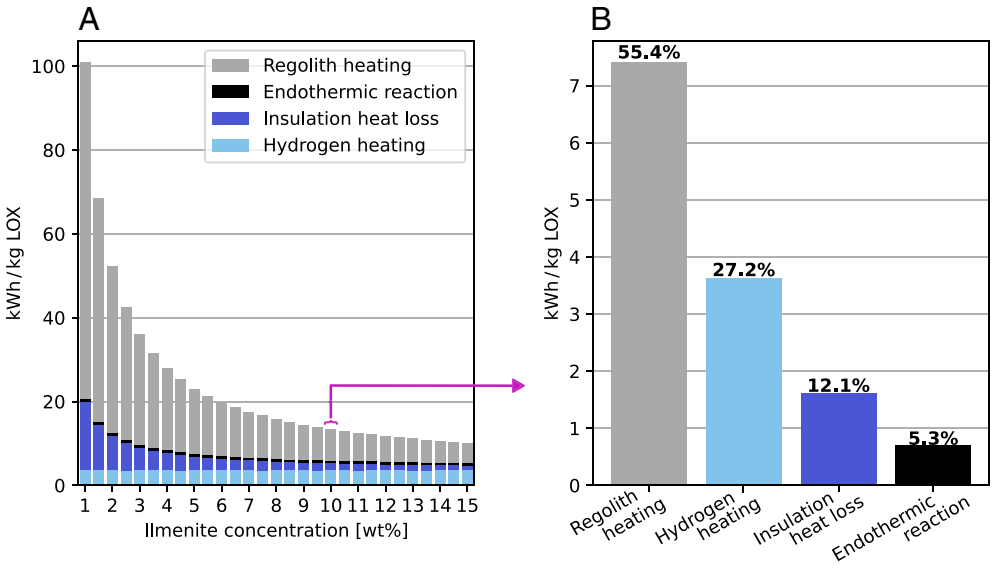

Fig. 3. Predicted hydrogen reduction reactor energy requirements comparison, (*A*) as a function of ilmenite concentration and, (*B*) at 10 wt% ilmenite concentration.

strongly depends on the ilmenite concentration, because with lower ilmenite wt%, more energy is wasted to heat the nonreactive regolith material. This relationship is shown in Fig. 3, which compares the different energy sinks in the hydrogen reduction reactor, (A) as a function of ilmenite concentration and, (B) using a fixed 10 wt% ilmenite concentration feedstock.

For each batch of regolith processed, the energy lost due to insulation heat loss remains constant, but since more LOX is produced for higher ilmenite wt%, the energy required per kg LOX decreases with higher ilmenite wt%. Contrarily, the energy expended for heating hydrogen and sustaining the endothermic reduction reaction increases with higher ilmenite wt%, but LOX production also increases, resulting in a constant energy expenditure per kg LOX. Overall, the energy required per kg LOX decreases significantly for higher initial ilmenite concentration.

Next, the relationship between ilmenite concentration and energy cost per kg LOX is geographically represented on the lunar surface, as shown in Fig. 4. We emphasize that this representation is a rough approximation, which aims to illustrate the generalized geographic trends in energy requirements for this technology, even if the calculations are not based on comprehensive geotechnical parameters. The map shows the energy (kWh) required to produce 1 kg of LOX, with red being high cost, blue being low cost, and uncolored areas containing insufficient ilmenite to be considered. The map highlights the economic importance of the lunar equatorial regions for oxygen production via hydrogen reduction, and specifically the High-Ti Mare regions, which exhibit the lowest energy requirements. Three Mare locations are depicted which exhibit favorable energy requirements.

To generate Fig. 4, we first use the TiO_2 map provided by Lunar Reconnaissance Orbiter Camera (LROC) (47). Then, we use a regression to convert TiO_2 wt% into ilmenite wt% described in the study of Coman et al. (ilmenite wt% = 1.06 × total TiO_2 wt% − 0.16) (48). The regression is only suitable where TiO_2 is above 2 wt% (48). This regression implies that ~50% of TiO_2 occurs in nonilmenite minerals (such as augite, rutile, spinel, and armalcolite). Although the regression could be adjusted with differing soil maturity (48), such level of detail is beyond the scope of this study

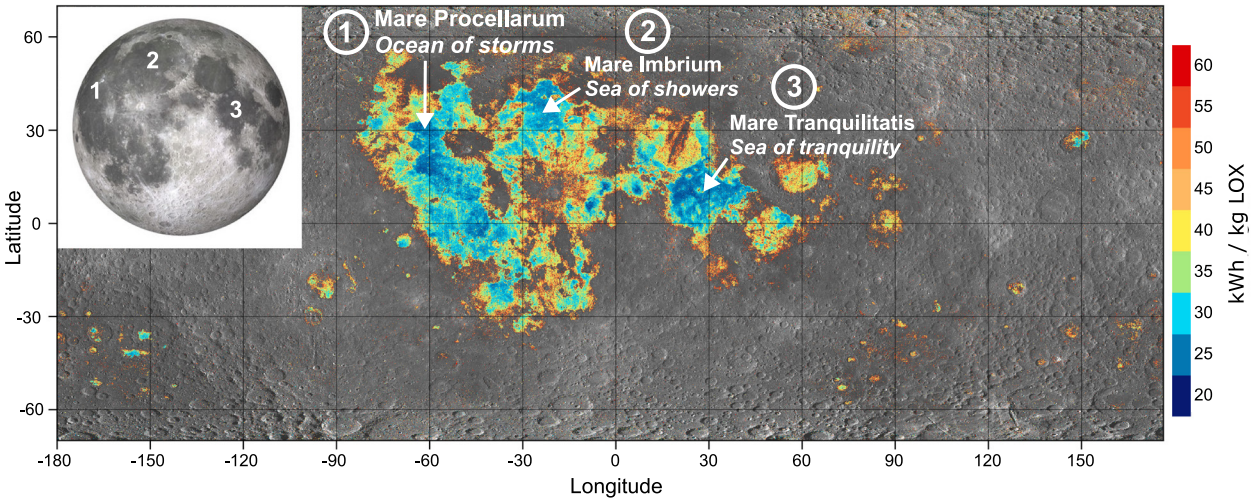

Fig. 4. Energy per kg LOX mapped onto the lunar surface depending on ilmenite wt%. The 2D lunar surface is depicted from +75 to −75 degrees latitude. The color coding shows the lower energy requirements (blue being favorable) to higher energy requirements (red being unfavorable) for LOX production. The resolution of the data is 400 m/pixel. Gray areas without color coding depict regions where ilmenite wt% are expected to be below 2%, which are not considered. Ilmenite wt% is thresholded to a maximum value of 15%, because higher concentrations are usually found in less easily exploited solid ores as opposed to granular materials. The spherical Moon on the *Top Left* identifies the position of the three Mare locations, and does not occlude any data.

and is not considered here. Furthermore, the grain size of the regolith particles, which can impact both beneficiation efficiency and the fraction of ilmenite that is reactive, is not included as a parameter in this model. Therefore, our study uses the estimate that 10 wt% TiO_2 in regolith is equivalent to ~10.4 wt% ilmenite. We note that TiO_2 concentration data from LROC is unavailable when concentration is below 2% and when latitude is beyond ± 75 degrees. Hence, the map displayed in Fig. 4 does not have an energy layer for such areas. Furthermore, ilmenite concentrations above 15 wt% likely correspond to ores contained in basalt rocks (49), whereas less than 15 wt% is common in loose granular material. As rocky feedstocks require specialized machinery that are not well characterized yet for lunar applications, these are not considered in this study. Therefore, we threshold all ilmenite concentration above 15 wt% on the map to a maximum value of 15 wt%.

The regression used provides a rough approximation of ilmenite concentration, and can be inaccurate for certain localized geology, for example pyroclastic deposits. Researchers have grouped local pyroclastic deposits (LPDs) into three classes (50) and Gaddis et al. mapped 75 LPDs (51) on the lunar surface. Of the different LPDs, the regression is expected to overestimate ilmenite for LPDs that contain substantial nonilmenite TiO_2 carriers, such as pyroxenes and glasses. On the other hand, some regional dark mantling deposits could contain significant ilmenite and have been identified as valuable targets for lunar bases, such as Taurus-Littrow, Rima Bode, Southern Mare Vaporum, and Southern Sinus Aestuum (50, 52). However, given that ilmenite occurs in various petrographical forms in these areas, the effectiveness of beneficiating and reacting the ilmenite from these resources remains to be determined. In this study, we do not distinguish petrographical impacts (such as grain size, presence of beads, and the association of ilmenite with olivine) on the beneficiation and reaction efficiency. In the future, more orbital, ground, and experimental processing data will become available to increase the accuracy of resource viability maps such as the one presented in this work.

Sensitivity Analysis and Uncertainty. We perform a sensitivity and uncertainty analysis, where a total of 22 free and independent parameters are identified. Dataset S1F includes the parameter ranges, chosen values for the baseline model, and sensitivity metrics. For the sensitivity analysis, we set a fixed 10 wt% ilmenite concentration, varied one parameter at a time within its range while keeping the other parameters at their default values, and measured the model outputs. The five parameters which, given their min and max input values, had the largest impact on the model results are summarized in Table 1 and Fig. 5. For the unitless sensitivity metric in Table 1, we approximated the slope of the parameter impact, by dividing the percentage change from baseline in the model outputs by the percentage change from baseline in the inputs (Dataset S1F). The two most sensitive parameters are the enrichment factor and electrolyzer efficiency (increasing each will lower the total energy). Fig. 5 shows that the enrichment factor has a nonlinear impact on the model output. Furthermore, one can see that although the electrolyzer efficiency has a similar sensitivity (slope), the expected range is much smaller than for the enrichment factor.

Next, the systematic uncertainties in the energy utilization per kg LOX are estimated by Monte Carlo error estimation (53). A uniform distribution is used as a probability density function for each parameter, the values for each of the 22 parameters are simultaneously and independently drawn within the min and max values shown in Table 1 and Dataset S1F, and the simulations are performed N = 1,000 times for each of the 29 different ilmenite concentrations from 1 wt% to 15 wt%. The variability of these results for different ilmenite concentrations is depicted in Fig. 6.

Table 1. Sensitivity analysis summary table for the five most critical parameters

	Parameter values			Total energy at 10 wt% ilmenite (kWh/kg LOX)		Sensitivity metric (Δ% energy/Δ% input)
Parameter	min	utilized	max	min	max	
Enrichment factor (unitless)	1.5	6	10.5	53.43	20.44	−0.39
Batch reaction time (h)	0.5	2.5	4.5	21.00	25.95	0.12
Electrolyzer efficiency	50%	60%	70%	26.13	22.94	−0.38
Ceramic Fiber Insulation (cm)	0.02	0.06	0.10	23.38	25.23	0.06
Temp. of H_2 before the heater (K)	623	723	823	25.08	23.46	−0.24

In Table 2, the Monte Carlo analysis is used to determine the amount of energy expended in each process step. The sum of the interquartiles (IQRs) of each process divided by two is used to define the error range of the estimated energy use at 10 wt% ilmenite in this study, i.e., 24.3 (± 5.8) kWh/kg LOX.

Notably, the primary source of uncertainty in the hydrogen reduction process can be attributed to the variability in the enrichment factor within the upstream beneficiation process. The enrichment factor is defined as the beneficiation process' ilmenite wt% in output divided by the ilmenite wt% in the input. This parameter significantly influences the uncertainty associated with the hydrogen reduction process. The enrichment factor is identified as the most critical parameter in the model due to its high uncertainty and significant impact on the process with the highest energy consumption.

Discussion

This study presents an end-to-end energy consumption model for the production of liquid oxygen on the Moon via hydrogen reduction of ilmenite. The results indicate a strong dependence of the energy demand based on feedstock composition. The majority of energy in the production chain is allocated to the high temperature hydrogen reduction (~55%) and electrolysis steps (~38%). Within the hydrogen reduction step, heating of hydrogen consumes 27% of energy demanded and heating regolith consumes 55%. The sensitivity analysis identifies the enrichment factor associated with the beneficiation process as the most critical parameter for improving energy utilization.

This study indicates that the majority of energy is expended on the chemical reaction processes and comparatively less on the mechanical and physical state change steps. Specifically, the heating of regolith, hydrogen, and ilmenite to the reactive temperature of 900 °C uses the most energy in the system. The beneficiation step modeled here enriches ilmenite using electrostatic properties and uses little energy directly; however, it modifies the composition of feed sent to the reactor, which strongly influences overall energy expenditure. Therefore, this study shows that improved beneficiation can significantly decrease the energy requirements of LOX production. When the material transferred to the reactor contains higher ilmenite wt%, less energy is wasted on heating the nonreactive regolith material. Heating nonilmenite containing regolith is

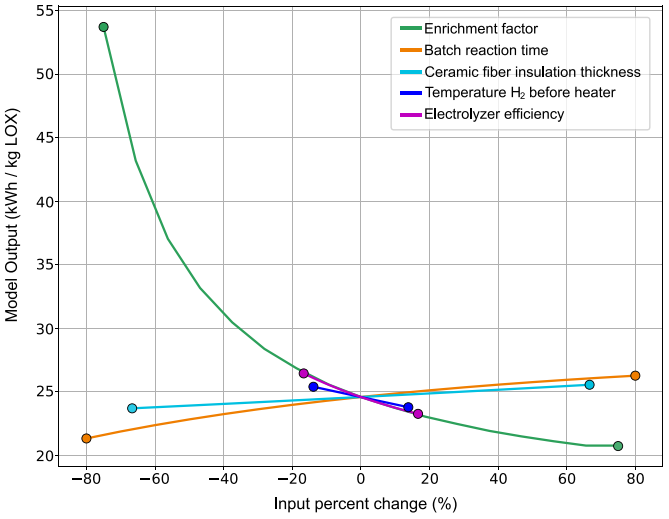

Fig. 5. Sensitivity analysis for baseline hydrogen reduction of ilmenite production chain using a 10 wt% ilmenite feedstock, individually varying the parameters to min and max values (Dataset S1F). The *x* axis represents the percent change of parameter inputs and the *y* axis represents the corresponding total energy use in kWh/kg LOX. The 5 out of 22 most important parameters are depicted based on which parameters cause the largest variations in model results over their range.

inefficient because it yields no oxygen and has higher specific heat capacity than ilmenite, requiring ~0.24 kWh/kg to go from 0 °C to 900 °C, compared to ilmenite requiring only ~0.21 kWh/kg.

Direct comparison of our results with other studies is challenging due to differences in technologies considered, assumptions, and methodologies. A literature review of energy estimations for lunar oxygen production is available in Dataset S1G. The review paper of Taylor and Carrier from 1993 (39) provided rough estimates for energy needs. They assumed an initial ilmenite concentration of 5 wt% with an enrichment factor of 10, and production scale of 1,000 tonnes/y. They do not state several other important parameters, such as the recovery rate of ilmenite in beneficiation. They estimate that the energy needed for hydrogen reduction of ilmenite is approximately 3 MW_{year} (~26 GWh), equivalent to 26 kWh/kg LOX, which is similar to our finding of 24.3 (±5.8) kWh/kg LOX. The same study also provides estimates for other technologies, which fall between 18 to 35 kWh/kg LOX. Their study states that this energy need represents the requirements to mine, transport, and process lunar ore, which leaves the precise definition of the envelope they considered ambiguous.

Kornuta et al. (9) investigated a system utilizing water-ice as the feedstock. They predict that producing 2,178 tonnes of LOX per year would require 2.8 MW, which is equivalent to 11.3 kWh/kg LOX. Their production chain includes sublimating ice, electrolysis, robotic systems, pumps, cryocoolers, heaters, communications, and lesser subsystems (9).

Some studies have developed end-to-end models for regolith-utilizing processes. Chen et al. studied space logistics optimization for Earth, Moon, and Mars transportation networks, and evaluated trade-offs in ISRU configurations (2). Considering the wide scope of their study, they present a simplified model of LOX energy consumption that does not consider regolith mineral composition as a parameter. They assumed that concentrated solar energy provides the main reactor heating energy demand, and so do not explicitly quantify the energy need for carbothermal and hydrogen reduction systems. They highlight that the storage size for LOX will depend on the frequency of launches, where higher launch frequency entails smaller storage needs. Guerro-Gonzalez and Zabel, present an end-to-end model for ISRU plants that produce metals with oxygen as a coproduct (45). Their study uses similar processing steps as ours but the results are not directly comparable because oxygen is a coproduct in their study. Furthermore their focus is on system mass instead of system energy use. They find that with a feed containing 7.5 wt% ilmenite and higher, hydrogen reduction outcompetes molten regolith electrolysis and molten salt electrolysis in terms of mass payback ratios.

This model is based on several simplifying assumptions and extrapolations from limited experimental data and can be improved as lunar exploration advances. Except for transportation, the other technologies considered in the production chain have yet to be demonstrated on the Moon. Hence, the results of the current model depend on limited experimental data (such as parabolic flight tests for electrostatic beneficiation), which may change in the future.

This current model assumes the excavator always works on the surface layer of the lunar regolith; however, it is possible to add excavation depth as a parameter. Additional data from the lunar surface about regolith geotechnical properties such as cohesion coefficient and soil density will improve modeling the energy consumption of excavators and transport systems. Furthermore, the impact of rocks and other impediments to excavators and transport systems, as well as real-world planned traverse paths that have specific topography and terrain types, could be added to future versions of the model. Notably, in the future, rail and other transport networks may be developed on the surface (54, 55).

The Moon's regolith varies in petrography, particle size distribution, maturity, and other characteristics based on geological soil formation processes (56). Hence formation processes can significantly impact the effectiveness of beneficiation, which could be reflected in future versions of this model. This model did not explicitly consider grain size separation in beneficiation. Sorting regolith by particle size can assist to dedust and remove coarse-grain materials, enrich the target mineral, and homogenize the feedstock which can improve the efficiency of both the mineral sorting beneficiation techniques and the hydrogen reduction reactor (57). Generally, larger particles have slower reaction rates and lower yield due to gas diffusion limitations as described in the shrinking core model (58, 59).

Our study confirms that beneficiation is an ISRU topic that requires additional research on process yields, energy requirements, available equipment, and performance in low gravity (21, 60). The importance of this knowledge gap is highlighted by the enrichment factor's large impact on the overall results of our

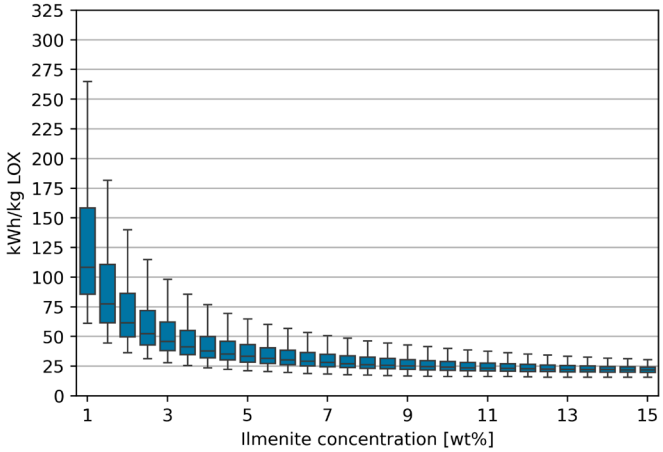

Fig. 6. Total energy required per kg LOX as a function of ilmenite concentration. The center lines in the boxes are the medians, the endpoints of the boxes are the Q1 and Q3 quartiles, and the endpoints of the whiskers are the minimum and maximum of the distributions excluding outliers.

Table 2. The median, Q1 (25% quartile), Q3 (75% quartile), and IQR (interquartile Q3 − Q1) of the different processes at 10 wt% ilmenite as evaluated by Monte Carlo simulations

Process	Median energy requirements (kWh/kg LOX)	Q1 (25% quartile) (kWh/kg LOX)	Q3 (75% quartile) (kWh/kg LOX)	IQR = Q3 − Q1 (Interquartile) (kWh/kg LOX)
Excavation	0.0022	0.0017	0.0031	0.0013
Transportation	0.15	0.11	0.20	0.089
Beneficiation	0.13	0.095	0.18	0.084
H_2 reduction	13.0	10.0	19.0	9.2
Electrolysis	9.4	8.6	10.0	1.6
Liquefaction	1.20	0.97	1.40	0.42
Storage	0.31	0.26	0.38	0.12

model. Using 10 wt% ilmenite and varying the enrichment factor from 1.5 to 10.5, the total energy consumption of the production chain varies from 53 to 23 kWh/kg LOX. While this study considered the use of electrostatic separation (*Methods*), several other methods have been described in the literature, including magnetic separation and electrostatic traveling wave (61–63). Furthermore, researchers are developing multistep beneficiation systems which use combinations of particle size sorting, magnetic, and electrostatic separation (57, 64).

Additional research is also needed regarding the impact of reactor temperature and operating pressure on reaction rates and product yield. In this case, yield is defined as oxygen product mass divided by input regolith mass. Increasing reactor temperature up to ~900 °C will increase yield, but at higher temperatures the yield curve is predicted to become asymptotic (27), however increasing temperature improves reaction rates until at least 1,100 °C (65). Higher operating pressure may lower reaction rates, due to products becoming trapped at the reactive surfaces of minerals (65). The impact of pressure on yield is unclear, some studies show that yield increases with lower pressure (27), while others show that yield decreases with lower pressure (44). Experimental data from reactors on the Moon will help to model specific reactor configurations, including batch sizes, durations, H_2/H_2O partial pressures, insulation, and the reactor heat exchange with the environment. Furthermore, more data on the processing of impurities in the lunar regolith will lead to more robust models. The numbers provided in the current work are designed to be a baseline that can be improved in future work as more information becomes available.

Another important assumption is how water from the reactor output is processed. We assumed passive cooling in a gas-separation unit to condensate water followed by proton-exchange membrane (PEM) electrolysis, but it is also possible to use direct vapor phase electrolysis with solid oxide electrolysis cells (SOEC). Since SOECs operate at temperatures higher than 800 °C, their implementation could circumvent the need for a water condensation step (27, 66). The water electrolysis system is presumed to have an energy efficiency penalty due to bubbles attaching to electrodes in lower gravity conditions (67). Given the energy demand for electrolysis is large, real-world experimental data from the Moon on this effect would improve the model accuracy.

Modeling the liquefaction step will benefit from more data about the Coefficient of Performance (COP) of cooling systems on the Moon. In addition, more data from agencies and private companies about the planned size and design of zero-boil off oxygen storage systems on the Moon will help improve the model. The duration of storage assumed here of 2 weeks (2 wk) could be updated with more information about the planned space transport architecture around oxygen production facilities.

For this analysis, the scale of production of 100 tonnes LOX/year is chosen and a single hydrogen reduction reactor with capacity for ~4 tonnes regolith per batch with a 2.5 h batch reaction duration is assumed. This scale is similar to the near-term lunar surface propellant demand estimated by Kornuta et al. (9). In the future, it is likely that several production sites operating in tandem, or scaled-up systems, would be needed since a single 100 tonne dry mass Starship HLS rocket without payload would already require an estimated minimum of ~80 tonnes LOX for a one-way trip to launch from the lunar surface to EML1 (*SI Appendix*). Furthermore, launches of Starship from Low Earth Orbit to Mars surface with up to 100 astronaut crew are expected to require approximately 860 tons of LOX (68). Alternatively, since a human uses ~300 kg of breathing oxygen per year, 100 tonnes LOX per year could support 333 astronauts (69).

The assumptions on production scale have important impacts on our model results. First, a smaller reactor size increases the surface area to volume ratio, which increases heat losses to the environment. Hence a larger reactor scale can improve energy efficiency. Meanwhile, a production chain using two smaller reactors in parallel could benefit from lower peak power requirements (44, 70) but suffer from lower overall energy efficiency.

Water-ice on the Moon is considered to be finite because the timescales of utilization could far outpace the timescales of regeneration (71). Furthermore, the water-ice resources are concentrated in geographically small regions of the Moon that may be hard to access (71). For these reasons, the exploitation of water-ice for the production of rocket propellant may become competitive, and contentious from a sustainability perspective. China, Russia, the European Union, India, and the United States, as well as private companies are aiming missions to the water-ice rich regions of the Moon's south pole. There is a risk that competition over these resources could cause interference in operations and spark legal conflicts (72) and international disputes (71). Thus, even if oxygen derived from oxide-bearing minerals in lunar regolith are more costly than oxygen from water-ice, the abundance and ubiquity of such oxides on the lunar surface offer important advantages. Furthermore, production of oxygen from oxides could be coupled to the production of useful metals (45).

We perform a rough approximation of the total theoretical lunar oxygen available on the Moon to make orders of magnitude comparisons (Dataset S1I). Note that these resources may not all be technically or economically exploitable. The predicted potential availability of oxygen is ~2.6 billion tonnes LOX from water-ice, compared to ~130 billion tonnes LOX from hydrogen reduction of ilmenite, and ~150 trillion tonnes LOX from total oxides. Since the initial Mars colonization effort of SpaceX aims to launch ~10,000 Starships to Mars (8), and assuming that lunar LOX is used for one-way trips that refuel at a Mars base, then ~10 Mtonnes (10 million tonnes) of LOX are needed in EML1 for the effort, which implies approximately 40 Mtonnes of LOX at the lunar base for launching this LOX to EML1 (i.e., 4:1 propellant to payload ratio for two-way trips from Moon surface to EML1) (15). Hence, the total lunar LOX demand for this Mars colonization effort can be roughly estimated at 50 Mtonnes. Using this estimate, completing the initial SpaceX Mars colonization plan of bringing 1 million humans to the Mars base could consume ~2% of the predicted total lunar water-ice resource. However, much of the water-ice may not be economically exploitable. In the future, the space economy may run out of easily exploitable lunar water and thus oxide-based oxygen production could become a more sustainable alternative.

In conclusion, the Moon is expected to play a key role in the supply of oxygen for the space economy (73) and this study provides valuable information on the energy requirements for the production of liquid oxygen on the Moon. The results of this study contribute to addressing Strategic Knowledge Gaps (17) identified by space agencies, and provide a foundation for future studies on oxygen production on the Moon. As more data become available, the modular nature of this model allows parameters to be updated to reflect the latest experimental research. Furthermore, future studies could build on this study to compare the end-to-end production chains of alternative oxygen production strategies. Finally, more key performance indicators beyond energy consumption can be added, such as mass payback ratios (45) and techno-economic analysis. Overall, this study presents a model which will support the space industry in evaluating the economic viability of technologies and locations for lunar oxygen production.

Methods

Overview Regolith to Oxygen. In this section, the overall modeling framework is introduced before presenting the modeling approach for the individual process steps. The modeling is implemented in Python, and is available on our github repository (74). The mass yield of the whole chain is solved first, prior to the energy usage. To solve the mass yield of LOX per kg regolith, we considered the mass and composition of inputs and outputs of each step in the production chain. The mass yield can then be calculated as shown in Eq. **1**.

$$Mass\ yield = \frac{m_{O2}}{m_{regolith}} = \frac{Ilmenite\ recovery\% \times ilmenite\ conversion\% \times head\ grade\% \times M_{O2}}{2 \times M_{Ilmenite}}, \quad [1]$$

Where m_{O2} is the mass of liquid oxygen produced, $m_{regolith}$ is the mass of initial excavated regolith, ilmenite recovery % is defined as the mass of ilmenite recovered after beneficiation divided by the mass of ilmenite fed to beneficiation (taken as 51%), ilmenite conversion % is the mass of ilmenite that is reacted in the hydrogen reactor divided by the mass of ilmenite fed to the reactor (taken as 47%), head grade % is concentration of ilmenite in excavated regolith (1 to 15%), M_{O2} is the molar mass of oxygen, and $M_{ilmenite}$ is the molar mass of ilmenite.

The energy requirements for oxygen production are calculated by accounting for the energy needed in each production step. The general approach taken for calculating these energy needs is described below. First, the energy demand parameters for each module are determined independently of mass flow. These represent the energy used per mass input into the process step. Next, the mass flow inputs and outputs throughout the production chain are calculated. To calculate the energy used per process step ($E_{Process\ step}$), we multiply the process energy demand parameter ($P_{Process\ step}$) by the actual mass input (m_{Input}) into each module as shown in Eq. **2**. The equation varies slightly for the excavation and beneficiation steps. The energy requirements for auxiliary equipment regarding the interfaces between the process steps are assumed to be negligible. Potential auxiliary equipment is listed in Dataset S1H.

$$E_{Process\ step} = P_{Process\ step} \times m_{Input}, \quad [2]$$

Next, the energy used per module ($E_{Excavation}$, $E_{Transportation}$, etc.) is divided by the net mass of liquid oxygen produced. This results in the energy per kg LOX of each module. Summing these, the process chain's total energy per kg LOX (E_{Total}) is obtained as given by Eq. **3**.

$$E_{Total}[kWh/kgLOX] = \frac{E_{Excavation} + E_{Transportation} + E_{Beneficiation} + E_{Reactor} + E_{Electrolysis} + E_{Liquefaction} + E_{Storage}}{m_{LOX}}, \quad [3]$$

Excavation. The first step in the production chain is excavating the lunar regolith. The modeled excavator is based on the Regolith Advanced Surface Systems Operations Robot (RASSOR) 2.0 developed by NASA (75). To calculate the energy requirements for excavation, the excavation force $F_{Excavation}$ is calculated first (Dataset S1A) and then multiplied by the distance traversed by the excavation tool $d_{bucket\ drum}$. To estimate the excavation mechanics of a RASSOR-style excavator, we model the excavation implement as a bucket in the formulation of Balovnev (76, 77). The bucket equations from that model are used with terms related to bucket drum geometry modified or simplified to account for the RASSOR geometry. Two main assumptions are made when formulating the excavation force model. First, the bucket portions of the RASSOR bucket drums are assumed to be not fully buried in the regolith, avoiding taking into account the additional force of lifting the regolith due to bucket drum rotation. To this end, an excavation depth of 2.5 cm is assumed. Second, RASSOR bucket drums are rotated about eight times faster than the wheels during trench-digging operation to avoid a rough surface finish. This yields the distance the bucket drums rotate $d_{Bucket\ drum}$, which is multiplied by the excavation force $F_{Excavation}$ and divided by the mass of regolith excavated $m_{Regolith\ excavated}$. To obtain the energy demand parameter, $P_{Excavation}$ as expressed in Eq. **4**, the energy requirements for overcoming the roll resistance must be added. For that, the power $P_{Vehicle}$ (Eq. **6**) for traveling at the digging velocity $v_{Digging}$ is multiplied by the digging distance $d_{Digging}$ and divided by $m_{Regolith\ excavated}$ and $v_{Digging}$.

$$P_{Excavation} = \frac{F_{Excavation} \times d_{Bucket\ drum}}{m_{Regolith\ excavated}} + \frac{P_{Vehicle} \times d_{digging}}{m_{Regolith\ excavated} \times v_{Digging}} = 6.5 \times 10^{-6} \frac{kWh}{kg}, \quad [4]$$

$P_{Excavation}$ is then multiplied by the amount of regolith excavated, which results in the energy needed for excavation $E_{Excavation}$ as described in Eq. **5**.

$$E_{Excavation} = P_{Excavation} \times m_{Regolith}, \quad [5]$$

Transportation. Next raw material from the excavation site is transported to the location where beneficiation takes place. The regolith is assumed to be transported by a vehicle similar to the RASSOR 2.0 (75). Moreover, this vehicle is assumed to travel on a flat surface and carry as much regolith as possible from the excavation site to the beneficiation site. During the outward trip to the excavation site, the rover is assumed to be empty. In order to estimate the energy cost of transportation, a semiempirical model is used based on Terramechanics (the science that studies the interaction of wheeled or tracked vehicles on various soils) (78). This model takes three sets of parameters as inputs (soil, vehicle, and wheel parameters) and computes the torque to be exerted on a wheel so that its traction effort compensates for its compaction resistance. This torque allows a vehicle with a given mass to travel at a constant speed on a flat surface. This torque can be multiplied with the wheel rotation speed to get the power required at wheel level P_{Wheel}. Finally, the power $P_{Vehicle}$ required for the vehicle to travel at a speed v is obtained by summing the power required by each wheel and taking into account the efficiency η of the electric motor and the transmission gears (Eq. **6**).

$$P_{Vehicle} = \frac{\left(2 \times P_{Wheel,front} + 2 \times P_{Wheel,rear}\right)}{\eta}, \quad [6]$$

The power required still depends on the mass of the vehicle and hence on the mass of the regolith conveyed. Thus, the power required by the empty rover for the outward trip $P_{Outward\ trip}$ (to the excavation site), is lower than the power required for the return trip $P_{Return\ trip}$ (to the beneficiation site). Considering a round-trip, Eq. **7** expresses the energy demand per kilogram of regolith and the distance transported, denoted as $P_{Transportation}$. The energy cost of the transportation module $E_{Transportation}$ as shown in Eq. **8**, can then be obtained by multiplying $P_{Transportation}$ with the mass of regolith transported $m_{Regolith}$ and the distance transported d (assumed to be 1 km). A detailed description of this work can be found in Dataset S1B.

$$P_{Transportation} = \frac{P_{Outward\ trip} + P_{Return\ trip}}{m_{Regolith} \times v} = 3.6 \times 10^{-4} \frac{kWh}{kg\ km}, \quad [7]$$

$$E_{Transportation} = P_{Transportation} \times m_{Regolith} \times d, \quad [8]$$

Beneficiation. Following transportation, the regolith will be beneficiated to produce a feed of consistent grade for subsequent processing. In this study, we modeled an electrostatic beneficiation system. Electrostatic beneficiation is chosen for this model for three primary reasons: First, electrostatic methods tend to require relatively little power consumption (21); second, compared to methods such as magnetic separation, they tend to be much less mass-intensive, making them more attractive from a launch cost perspective (21); and third, electrostatic beneficiation has been studied the most broadly in the literature, providing a more comprehensive dataset to base our calculations. Two main parameters are identified from the literature: the enrichment factor and ilmenite recovery. The values employed here are determined by reviewing those found in the literature (Dataset S1C) (79–81). The enrichment factor is defined as the ratio of the ilmenite concentrate grade divided by the head grade. Based on the data from Agosto (79), Quinn et al. (80), and Oder (81) we assumed an enrichment factor of 6. The ilmenite recovery, measured in weight-percent (wt%), is defined as the ratio of ilmenite mass in the concentrate divided by the ilmenite mass in the initial feedstock. Again, from the data available in the literature, we took the ilmenite recovery for an electrostatic beneficiation process to be 50.5%. We assume that the ilmenite head grade does not exceed 15 wt%, and that the maximum concentrate grade is 99 wt% ilmenite. Eq. **9** gives the mass of postbeneficiation ilmenite, and Eq. **10** gives the mass of postbeneficiation regolith, which includes gangue.

$$m_{Beneficiated\ ilmenite} = m_{regolith} \times Ilmenite\ \ recovery\,\% \times head\ \ grade\,\%, \quad [9]$$

$$m_{Beneficiated\ regolith} = \frac{m_{Beneficiated\ ilmenite}}{enrichment\ \ factor \times head\ \ grade\,\%}, \quad [10]$$

The beneficiation process significantly impacts the mass flow of the model. However, the energy consumption in electrostatic separation is negligible relative to other process units in the model and is therefore neglected. Note that we assume no particle size separation step, and furthermore this model does not consider processes that include crushing rocks. If other more energy-intensive beneficiation methods are to be used, then that energy would in fact need to be accounted for. Nevertheless, we include energy expenditure for the transportation and handling of regolith in this step as per Eq. **11**. The mass of the transported regolith is assumed to be lifted by 1 m in height (h) at the beneficiation site and the waste material that is leftover during beneficiation (gangue) is assumed to be transported away from the beneficiation site by 1 km (d), followed by the return of the empty rover.

$$E_{Beneficiation} = m_{Regolith} \times g_{Lunar} \times h + m_{Gangue} \times P_{Transportation} \times d \quad [11]$$

Hydrogen Reduction Reactor. Following beneficiation, the enriched regolith is conveyed to the hydrogen reduction reactor. In the reactor, the beneficiated regolith is heated to 900 °C and reacted with hydrogen gas at an operating pressure of 1 bar. The ilmenite in the regolith is reduced by hydrogen to produce water, iron, and titanium dioxide (82), an idealized version of this reaction is shown in Eq. **12**.

$$H_2 + FeTiO_3 \rightarrow H_2O + Fe + TiO_2, \quad [12]$$

The reactor operation is assumed to consist of four phases with specific time intervals: regolith loading (0.5 h), heat-up (5 h), batch reaction (2.5 h), and regolith unloading (0.5 h) (70, 83). The modeled reactor is based on a spherical fluidized bed reactor operating in batch mode (44), and is assumed to operate continuously with 100% uptime. A schematic of the reactor model during the reaction phase is depicted in Fig. 7. The yield of water m_{H_2O} from this process is described in Eq. **13**, where the ilmenite conversion % (ic%) represents the ratio of ilmenite that reacts with hydrogen and is converted to H_2O, Fe, and TiO_2.

$$m_{H_2O} = m_{Beneficiated\ ilmenite} \times ic\% \times \frac{m_{H_2O}}{M_{Ilmenite}}, \quad [13]$$

The energy needed to operate the reactor includes heating the regolith, heating input hydrogen flow, insulation heat loss, and the energy needed to sustain the endothermic reduction reaction. Summing these values and dividing by the mass of regolith inside the reactor results in the parameter $P_{Reactor}$ as expressed in Eq. **14**, which is the energy consumed by the reactor per kg regolith. However, $P_{Reactor}$ is not constant, since it depends on the ilmenite % of the input regolith batch. The reactor energy $E_{Reactor}$ is obtained by multiplying $P_{Reactor}$ with the mass of the regolith $m_{Beneficiated\ regolith}$ passed into the reactor module as shown in Eq. **15**.

$$P_{Reactor} = 0.385 \pm 0.085 \frac{kWh}{kg_{regolith}}, \quad [14]$$

$$E_{Reactor} = P_{Reactor} \times m_{Beneficiated\_regolith}, \quad [15]$$

The estimation of the reactor's size is based on the assumption of producing 100 tonnes of oxygen annually (23). This results in a regolith batch mass of 3,861 kg. After the reactor size and batch mass is estimated, the energy to heat the regolith from 0 °C (average temperature between day and night side) (70) to 900 °C (31) is calculated using the heat capacity of regolith (84) and ilmenite (85). Since the two heat capacity curves differ, the energy to heat up the regolith is determined based on the ilmenite wt%. After the reaction, the hot reacted solid material is removed from the reactor. The present study does not consider heat recovery from regolith removed from the reactor. The modeled reactor consists of an inner layer of Ceramic Fiber Insulation (CFI) (86) and an outer layer of High-Temperature Multi-Layer Insulation (HTMLI) (83) (87). Both are assumed to be 6 cm thick (44). The heat loss is calculated by doing a radiative heat balance around the outer reactor surface for the heat-up and reaction phases (Dataset S2E). Additional heat is lost to reheating the cooled-down insulation after the regolith unloading and loading phases. Here, the insulation is assumed to cool down by 200 °C on average. Heat losses in pipes and mechanical supports as well as heat losses during regolith loading and unloading phases are neglected.

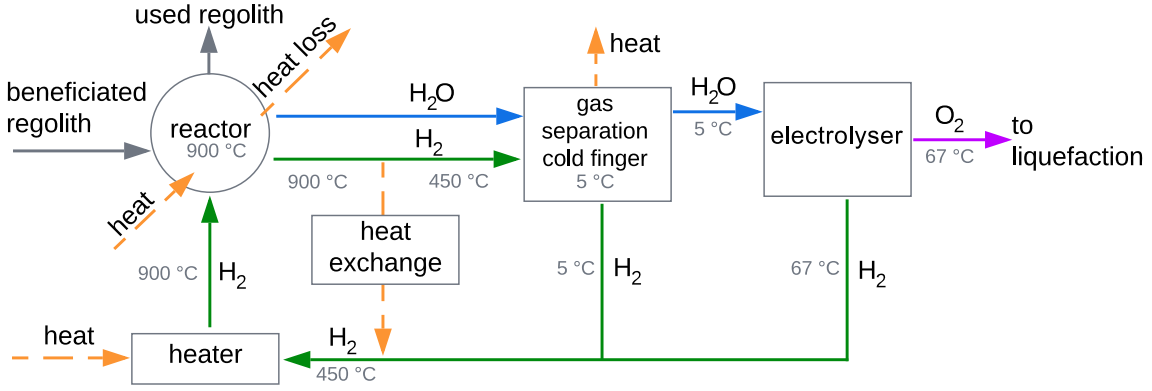

Fig. 7. Schematic of the reactor model during the reaction phase, showing the hydrogen loop and water/oxygen mass flows.

The required hydrogen mass flow is calculated to determine the energy needed to heat the hydrogen to reaction temperature. To drive forward the reaction, water must be continuously removed from the reaction chamber. Since it is recommended that the molar ratio of H_2O vapor to H_2 should stay below 10% (31), a ratio of 1% is assumed as the operating point of the reactor. Thus, the output gas contains a substantial amount of unreacted hydrogen mixed in with the desirable water vapor output. For higher ilmenite concentrations, more water is produced, resulting in a higher water mass flow out of the reactor. This demands higher hydrogen input mass flow to maintain the desired molar ratio in the output gas. The hydrogen from the gas separation unit and the electrolyzer is first reheated to 450 °C in a heat exchanger, which moves thermal energy from the hot output gas of the reactor to the hydrogen input gas. In the second step, hydrogen is heated to 900 °C in a heater unit before entering the reactor (Dataset S2F). No loss of water or hydrogen in the condensation and recycling process is assumed. To determine how much ilmenite reacts during the reaction phase, data from ref. 70 is used, which quantifies ilmenite conversion % depending on reaction time (Dataset S2C). Here, it is assumed that the water mass flow out of the reactor remains constant during the reaction phase. Additionally, energy requirements for the operation of the pumps and other auxiliary systems are neglected. The power demand required to cool gasses and condensate water in the gas separation unit is not included in this model, but a back of the envelope estimate of power demand for this unit operation indicates consumption of less than 1 kWh/kg LOX (Dataset S1J).

Electrolysis. Following the hydrogen reduction reactor, the condensed water is transferred to an electrolyzer. In this step, water is split into hydrogen and oxygen using a PEM electrolyzer. Eq. **16** shows the oxygen output of the electrolysis module.

$$m_{O2} = \frac{m_{H_2O} \times M_{O_2}}{2 \times M_{H_2O}}, \quad [16]$$

The modeled electrolyzer is based on PEM electrolysis with a system efficiency of 60% (88). However, due to the slower rising of gas bubbles at the electrodes in lunar gravity compared to earth gravity, electrolysis could be 11% less efficient on the Moon (67). This results in a total electrolyzer efficiency η_{total} of 53.4%. With that, the electrolysis energy per kg H_2O, $P_{Electrolysis}$, can be calculated as expressed in Eq. **17**. First, we consider the energy content of hydrogen, E_{H2}, taken as 39.7 kWh/kg (89) with its molar mass and divide that by the total electrolyzer efficiency η_{total} and the molar mass of water. The energy for electrolysis $E_{Electrolysis}$ is obtained by multiplying $P_{Electrolysis}$ with the mass of water m_{water} passed into the electrolysis module as shown in Eq. **18**.

$$P_{Electrolysis} = \frac{E_{H_2} \times M_{H_2}}{\eta_{total} \times M_{H_2O}} = 8.26 \frac{kWh}{kg_{H_2O}}, \quad [17]$$

$$E_{Electrolysis} = P_{Electrolysis} \times m_{water}, \quad [18]$$

Liquefaction. After electrolysis, the next step is liquefaction. A cryocooler is used to cool oxygen down to its boiling point and then liquefy it. The modeled cryocooler is based on a Turbo-Brayton cryocooler (90) with an efficiency, $\eta_{cryocooler}$, of 20% compared to the Carnot efficiency (91). To calculate the COP of the utilized cryocooler (92), the COP-Carnot, which is the maximum theoretical efficiency, must be calculated first. It depends on the temperature of the cold and hot reservoirs of the system and is given by Eq. **19**.

$$COP_{Carnot} = \frac{T_{cold}}{T_{hot} - T_{cold}}, \quad [19]$$

The temperature of the cold reservoir is assumed to be 80 K, since it must be lower than the boiling point of oxygen (~90 K at the assumed pressure of 1 bar), to remove heat and liquefy it. The cryocooler's working fluid accepts the heat and rejects it at the hot reservoir of the cryocooler. This hot reservoir is assumed to be an array of radiators, radiating the heat into outer space. The temperature of the hot reservoir is the temperature of the radiators and is assumed to be 233 K, based on the temperature of the radiators on the ISS (93). The liquefaction module calculates $P_{Liquefaction}$, which is the energy needed to liquefy 1 kg of O_2. More specifically as formulated in Eq. **20**, it is the heat that needs to be removed from the oxygen to cool it down from T_{in} to T_{out} and then liquefy it. This value is divided by the COP of the cryocooler, which is the COP-Carnot multiplied by the efficiency of the cryocooler. Eq. **21** then calculates $E_{Liquefaction}$ by multiplying $P_{Liquefaction}$ with the mass of oxygen passed into the liquefaction module.

$$P_{Liquefaction} = \frac{cp_{O_2} \times (T_{in} - T_{out}) + \Delta h_{vap,O_2}}{\eta_{cryocooler} \times COP_{Carnot}} = 1.17 \frac{kWh}{kg_{O_2}}, \quad [20]$$

$$E_{Liquefaction} = P_{Liquefaction} \times m_{oxygen}, \quad [21]$$

Storage. The produced liquid oxygen is stored in a cryogenic tank for a storage time of 2 wk. After that, it is assumed to be transferred to an ascent vehicle to be delivered in space. The storage tank is exposed to radiative heat flux from the sun, as well as conductive and radiative heat flux from the lunar surface. To prevent the produced LOX from warming up and boiling off (94), this heat leak needs to be removed (7). This is accomplished by employing a zero-boil-off (ZBO) system. It consists of a cryocooler placed on the outer wall of the tank, which constantly removes heat from the cryogenic tank (95). The modeled spherical tank with a diameter of 0.962 m is chosen based on how much LOX is produced in the storage time of 2 wk. The tank wall is made of a 4 mm thick stainless steel layer (96), and an insulation made up of vacuum-insulated-panels (VIP) with a thickness of 25 mm (97). The thermal conductivity of VIP is assumed to be 0.006 W/mK (98). The goal of the storage module is to calculate the energy needed to keep 1 kg of LOX in liquid state for 2 wk ($P_{Storage}$). First, the size and geometry of the LOX-tank is calculated, then the heat transfer coefficient between the LOX and the inner tank wall is determined (Dataset S3B). By considering radiative heat flux, as well as conductive heat flux through mechanical supports, an outer surface heat balance of the tank can be derived (Dataset S3D). The outcome of the heat balance is the heat flux into the LOX-tank, which the ZBO system must remove to keep the liquid oxygen from boiling off. The power consumption of the ZBO system is calculated by dividing the heat flux into the tank by the COP of the used cryocooler. The ZBO system's power consumption P_{ZBO_system} is multiplied by the storage time of 2 wk $t_{storage}$ and divided by the stored LOX mass $m_{LOX,\,stored}$ (Dataset S3E). This results in parameter $P_{Storage}$ as given by Eq. **22**. By multiplying $P_{Storage}$ with the input of mass of oxygen, the energy required for the storage module $E_{Storage}$ is obtained as per Eq. **23**.

$$P_{Storage} = \frac{P_{ZBO\_system} \times t_{storage}}{m_{LOX,stored}} = 0.31 \frac{kWh}{kg_{LOX}}, \quad [22]$$

$$E_{Storage} = P_{Storage} \times m_{oxygen}, \quad [23]$$

Data, Materials, and Software Availability. Python model, currently available on github. Will be moved to Open Science Framework upon publication data have been deposited in Github and later OSF (https://github.com/dlite-x/Space_resources_LEIA) (74).

ACKNOWLEDGMENTS. We thank Rodrigo Molina Dacaret for his talented work with Geographic Information Systems, Elad Noor for guidance on statistical analysis, Paolo Mangili for support on space logistics, and Francisco Guerrero Gonzalez, Aleksander Orzechowski, Dennis Harries, Hanna Sargeant, Beth Lomax, Prayag Parthak, Vittorio Rainaldi, Johanna Haffner, and Toby Call for their valuable insights. Funding was provided by the European Space Agency, and Cx Bio.

Author affiliations: [a]Spaceship, European Astronaut Center, Exploration Preparation, Research and Technology Team (ExPeRT), Directorate of Human and Robotic Exploration, European Space Agency, Cologne 51147, Germany; [b]Cx Bio, Luxembourg 2521, Luxembourg; [c]Future Mining Team, Commonwealth Scientific and Industrial Research Organisation, Mineral Resources, Clayton VIC 3168, Australia; [d]Department of Earth Science and Engineering, Imperial College London, London SW7 2AZ, United Kingdom; [e]Center for Space Resources, Colorado School of Mines, Golden, CO 80401, Colorado; [f]Spaceship FR, Centre National d'Etudes Spatial, Toulouse 31400, France; [g]Belgian Air and Space Component, Control & Reporting Centre, Belgian Armed Forces, Brussels 1140, Belgium; and [h]Karlsruhe Institute of Technology, Karlsruhe 76131, Germany

1. H. Köpping Athanasopoulos, The Moon village and space 4.0: The 'open concept' as a new way of doing space? *Space Policy* **49**, 101323 (2019).
2. H. Chen, T. Sarton du Jonchay, L. Hou, K. Ho, Integrated in-situ resource utilization system design and logistics for Mars exploration. *Acta Astronaut.* **170**, 80–92 (2020).
3. D. L. Linne *et al.*, "Overview of NASA technology development for in-situ resource utilization (ISRU)" in *68th International Astronautical Congress (IAC)* (2017). ntrs.nasa.gov/citations/20180000407. Accessed 15 January 2023.
4. A. Liu, Z. Shi, X. Hu, B. Gao, Z. Wang, Lunar soil simulant electrolysis using inert anode for Al–Si alloy and oxygen production. *J. Electrochem. Soc.* **164**, H126 (2017).
5. B. A. Lomax *et al.*, Proving the viability of an electrochemical process for the simultaneous extraction of oxygen and production of metal alloys from lunar regolith. *Planet. Space Sci.* **180**, 104748 (2020).
6. M.-A. Chavy-Macdonald, K. Oizumi, J.-P. Kneib, K. Aoyama, The cis-lunar ecosystem—A systems model and scenarios of the resource industry and its impact. *Acta Astronaut.* **188**, 545–558 (2021).
7. D. W. Plachta, W. L. Johnson, J. R. Feller, Zero boil-off system testing. *Cryogenics* **74**, 88–94 (2016).
8. P. T. Metzger, Economics of in-space industry and competitiveness of lunar-derived rocket propellant. *Acta Astronaut.* **207**, 425–444 (2023).
9. D. Kornuta *et al.*, Commercial lunar propellant architecture: A collaborative study of lunar propellant production. *REACH* **13**, 100026 (2019).
10. L. Siltala, M. Granvik, Asteroid mass estimation using Markov-chain Monte Carlo. *Icarus* **297**, 149–159 (2017).
11. S. Mouret, D. Hestroffer, F. Mignard, Asteroid mass determination with the Gaia mission: A simulation of the expected precisions. *Planet. Space Sci.* **56**, 1819–1822 (2008).
12. N. J. Bennett, R. Xie, A. G. Dempster, The Moon and NEAs as sources of cislunar propellant; removing some constraints from a recent paper drives down lunar sourced propellant cost. *Acta Astronaut.* **190**, 409–412 (2022).
13. B. Chehroudi, D. Talley, V. Yang, "Liquid propellants and combustion: Fundamentals and classifications" in *Encyclopedia of Aerospace Engineering* (John Wiley & Sons Ltd., 2010).
14. P. Calla, D. Fries, C. Welch, Asteroid mining with small spacecraft and its economic feasibility. arXiv [Preprint] (2018). https://doi.org/10.48550/arXiv.1808.05099 (Accessed 15 January 2023).
15. P. Mangili, "Space Tugs and Lagrange Points: Key architectures for the new Cis-Lunar economy" in *International Astronautical Congress 2023* (2023). afastro.directory/iac/paper/id/74762/summary/. Accessed 15 January 2023.
16. M. A. Gibson, C. W. Knudsen, "Lunar oxygen production from ilmenite" in *Lunar Bases and Space Activities of the 21st Century* (Lunar and Planetary Institute, 1985), p. 543.
17. International Space Exploration Coordination Group, "In-situ resource utilization gap assessment report". https://www.globalspaceexploration.org/wordpress/wp-content/uploads/2021/04/ISECG-ISRU-Technology-Gap-Assessment-Report-Apr-2021.pdf. Accessed 15 January 2023.
18. NASA's management of the Artemis missions (Report No. IG-22-003, Office of Inspector General, 15 November 2021), p. 73.
19. T. J. Colvin, K. Crane, B. Lal, Assessing the economics of asteroid-derived water for propellant. *Acta Astronaut.* **176**, 298–305 (2020).
20. J. J. Papike, S. B. Simon, J. C. Laul, The lunar regolith: Chemistry, mineralogy, and petrology. *Rev. Geophys.* **20**, 761–826 (1982).
21. J. N. Rasera, J. J. Cilliers, J. A. Lamamy, K. Hadler, The beneficiation of lunar regolith for space resource utilisation: A review. *Planet. Space Sci.* **186**, 104879 (2020).
22. M. F. McKay, D. S. McKay, M. B. Duke, *Space Resources Materials* (NASA Lyndon B Johnson Space Center, Houston, TX, 1992).
23. W. E. F. L. Moulford, A. R. Martin, P. W. Cains, P. D. Martin, G. B. T. Tan, A comparative evaluation of lunar oxygen production technologies. *SAE Trans.* **105**, 1053–1062 (1996).
24. G. H. Just, K. Smith, K. H. Joy, M. J. Roy, Parametric review of existing regolith excavation techniques for lunar In Situ Resource Utilisation (ISRU) and recommendations for future excavation experiments. *Planet. Space Sci.* **180**, 104746 (2020).
25. C. Meyer, *NASA Lunar Petrographic Educational Thin Section Set* (Astromaterials Curation NASA Lyndon B. Johnson Space Center, 2003).
26. G. H. Heiken, D. T. Vaniman, B. M. French, *Lunar Sourcebook, A User's Guide to the Moon* (Cambridge University Press, 1991).
27. B. H. Altenberg, "Oxygen production on the Lunar materials processing frontier" in *Proceedings of the Lunar Materials Technology Symposium, Arizona University* (Document ID 19930018778, 1992).
28. M. Shaw *et al.*, Mineral processing and metal extraction on the lunar surface–Challenges and opportunities. *Miner. Process. Extr. Metall. Rev.* **43**, 865–891 (2022).
29. L. Schlüter, A. Cowley, Review of techniques for in-situ oxygen extraction on the Moon. *Planet. Space Sci.* **181**, 104753 (2020).
30. R. Gustafson, E. Rice, "Lunar polar ice–Methods for mining the new resource for exploration" in *37th Aerospace Sciences Meeting and Exhibit*, Aerospace Sciences Meetings (American Institute of Aeronautics and Astronautics, 1999).
31. H. Sargeant *et al.*, Hydrogen reduction of lunar samples in a static system for a water production demonstration on the Moon. *Planet. Space Sci.* **205**, 105287 (2021).
32. S. Schreiner *et al.*, "Development of a molten regolith electrolysis reactor model for lunar in-situ resource utilization" in *8th Symposium on Space Resource Utilization* (American Institute of Aeronautics and Astronautics) (2015).
33. R. J. Gustafson, B. C. White, M. J. Fidler, Oxygen production via carbothermal reduction of lunar regolith. *SAE Int. J. Aerosp.* **4**, 311–316 (2009).
34. L. Karr *et al.*, "Ionic liquid facilitated recovery of metals and oxygen from regolith" in *2018 AIAA SPACE and Astronautics Forum and Exposition* (American Institute of Aeronautics and Astronautics) (2018).
35. G. B. Sanders, W. E. Larson, Progress made in lunar in situ resource utilization under NASA's exploration technology and development program. *J. Aerosp. Eng.* **26**, 5–17 (2013).
36. H. Sargeant, "Water from lunar regolith: Reduction by hydrogen for a small-scale demonstration of in situ resource utilisation for the Moon", PhD thesis, The Open University, United Kingdom (2020).
37. S. Barber *et al.*, "ProSPA: The chemical laboratory for in-situ assessment of lunar volatile resources within ESA's prospect package" in *European Lunar Symposium 2016* (Abstract #047, 2016). core.ac.uk/outputs/374157311/?source=2. Accessed 15 January 2023.
38. R. J. Williams, D. S. McKay, D. Giles, T. E. Bunch, Mining and beneficiation of lunar ores. *Space Resour. Space Settl.*, 188–275 (1979).
39. L. A. Taylor, W. D. Carrier III, "Oxygen production on the moon: An overview and evaluation" in *Resources of Near-Earth Space* (The University of Arizona Press, London, 1993), p. 69.
40. M. A. Gibson, C. W. Knudsen, "Lunar hydrogen recovery process."US Patent US4938946A (1990).
41. D. Heather *et al.*, "The ESA PROSPECT payload for Luna 27: Science activities and development" in *Europlanet Science Congress 2022* (EPSC2022-533, 2022), vol. 16. ui.adsabs.harvard.edu/abs/2022EPSC...16..533H/abstract. Accessed 15 January 2023.
42. D. Urbina *et al.*, "ALCHEMIST-ED: European earth-based demonstrator of production of water from lunar regolith" in *International Astronautical Congress* (2022). iafastro.directory/iac/paper/id/69399/summary/. Accessed 12 January 2023.
43. U. Hegde, R. Balasubramaniam, S. Gokoglu, "Heating-rate coupled model for hydrogen reduction of JSC-1A" in *48th AIAA Aerospace Sciences Meeting Including the New Horizons Forum and Aerospace Exposition* (American Institute of Aeronautics and Astronautics) (2010).
44. D. Linne, "Employing ISRU Models to Improve Hardware Designs" in *48th AIAA Aerospace Sciences Meeting Including the New Horizons Forum and Aerospace Exposition*, Aerospace Sciences Meetings (American Institute of Aeronautics and Astronautics, 2010).
45. F. J. Guerrero-Gonzalez, P. Zabel, System analysis of an ISRU production plant: Extraction of metals and oxygen from lunar regolith. *Acta Astronaut.* **203**, 187–201 (2022), 10.1016/j.actaastro.2022.11.050.
46. G. Jamanca-Lino, Space resources engineering: Ilmenite deposits for oxygen production on the Moon. *Am. J. Min. Metall.* **6**, 6–11 (2022).
47. H. Sato *et al.*, Lunar mare TiO2 abundances estimated from UV/Vis reflectance. *Icarus* **296**, 216–238 (2017).
48. E. O. Coman, B. L. Jolliff, P. Carpenter, Mineralogy and chemistry of Ti-bearing lunar soils: Effects on reflectance spectra and remote sensing observations. *Icarus* **306**, 243–255 (2018).
49. J. G. Chambers, L. A. Taylor, A. Patchen, D. S. McKay, Quantitative mineralogical characterization of lunar high-Ti mare basalts and soils for oxygen production. *J. Geophys. Res. Planets* **100**, 14391–14401 (1995).
50. S. J. Lawrence, B. R. Hawke, "Lunar pyroclastic deposits: An accessible and quantifiable lunar resource" in *39th Lunar and Planetary Science Conference* (LPI Contribution No. 1391, 2008). www.lpi.usra.edu/meetings/lpsc2008/pdf/1804.pdf. Accessed 15 January 2023.
51. L. R. Gaddis, M. I. Staid, J. A. Tyburczy, B. R. Hawke, N. E. Petro, Compositional analyses of lunar pyroclastic deposits. *Icarus* **161**, 262–280 (2003).
52. B. R. Hawke, C. R. Coombs, B. Clark, "Ilmenite-rich pyroclastic deposits: An ideal lunar resource" in *Lunar and Planetary Science Conference* (Accession Number 90A33477, 1990). adsabs.harvard.edu/full/1990LPSC...20..249H. Accessed 15 January 2023.
53. E. Koehler, E. Brown, S.J.-P.A. Haneuse, On the assessment of Monte Carlo Error in simulation-based statistical analyses. *Am. Stat.* **63**, 155–162 (2009).
54. E. Schaler, *Flexible levitation on a track (FLOAT)* (NASA, 2024).
55. Northrop Grumman to Develop Concept for Lunar Railroad (Northrop Grumman Newsroom, 2024).
56. D. S. McKay *et al.*, "The lunar regolith" in *Lunar sourcebook* (Cambridge University Press, Cambridge, United Kingdom, 1991), pp. 285–356.
57. M. Berggren, R. Zubrin, P. Jonscher, J. Kilgore, "Lunar Soil Particle Separator" in *49th AIAA Aerospace Sciences Meeting Including the New Horizons Forum and Aerospace Exposition*, Aerospace Sciences Meetings (American Institute of Aeronautics and Astronautics, 2011).
58. U. Hegde, R. Balasubramaniam, S. Gokoglu, Development of a reactor model for chemical conversion of lunar regolith. *AIP Conf. Proc.* **880**, 941–950 (2007).
59. L. Schlüter, A. Cowley, Review of techniques for In-Situ oxygen extraction on the Moon. *Planet. Space Sci.* **181**, 104753 (2020).
60. J. J. Cilliers, J. N. Rasera, K. Hadler, Estimating the scale of Space Resource Utilisation (SRU) operations to satisfy lunar oxygen demand. *Planet. Space Sci.* **180**, 104749 (2020).
61. X. Yang *et al.*, Triboelectric properties of ilmenite and quartz minerals and investigation of triboelectric separation of ilmenite ore. *Int. J. Min. Sci. Technol.* **28**, 223–230 (2018).
62. H. Kawamoto, Some techniques on electrostatic separation of particle size utilizing electrostatic traveling-wave field. *J. Electrost.* **66**, 220–228 (2008).
63. M. Adachi, H. Moroka, H. Kawamoto, S. Wakabayashi, T. Hoshino, Particle-size sorting system of lunar regolith using electrostatic traveling wave. *J. Electrost.* **89**, 69–76 (2017).
64. K. Kulkarni, M. Fabien Franke, M. I. Jundullah Hanafi, T. M. Gesing, P. Zabel, Optimizing lunar regolith beneficiation for ilmenite enrichment. *Front. Space Technol.* **4**, 1328341 (2024).
65. H. M. Sargeant *et al.*, Hydrogen reduction of ilmenite: Towards an in situ resource utilization demonstration on the surface of the Moon. *Planet. Space Sci.* **180**, 104751 (2020).
66. A. Pandiyan, A. Uthayakumar, R. Subrayan, S. W. Cha, S. B. Krishna Moorthy, Review of solid oxide electrolysis cells: A clean energy strategy for hydrogen generation. *Nanomater. Energy* **8**, 2–22 (2019).
67. B. A. Lomax *et al.*, Predicting the efficiency of oxygen-evolving electrolysis on the Moon and Mars. *Nat. Commun.* **13**, 583 (2022).
68. S. Fälker *et al.*, "Modular ISRU systems as a building block for sustainable space exploration" in *73rd International Astronautical Congress (IAC)* (2022). iafastro.directory/iac/paper/id/69607/summary/. Accessed 15 January 2023.
69. M. Ewert, "Astronaut mass balance for long duration missions" in *49th International Conference on Environmental Systems* (ICES-2019-126, 2019). ntrs.nasa.gov/api/citations/20190027563/downloads/20190027563.pdf. Accessed 15 January 2023.
70. D. Linne *et al.*, "Component and system sensitivity considerations for design of a lunar ISRU oxygen production plant" in *47th AIAA Aerospace Sciences Meeting* (2009) ntrs.nasa.gov/api/citations/20120012846/downloads/20120012846.pdf. Accessed 15 January 2023.
71. M. Elvis, A. Krolikowski, T. Milligan, Concentrated lunar resources: Imminent implications for governance and justice. *Philos. Trans. R. Soc. Math. Phys. Eng. Sci.* **379**, 20190563 (2020).
72. Disputes over space mining on the horizon? https://www.ibanet.org/disputes-over-space-mining-on-the-horizon. Accessed 17 January 2024.
73. D. L. Linne *et al.*, Lunar production system for extracting oxygen from regolith. *J. Aerosp. Eng.* **34**, 04021043 (2021).
74. D. Leger *et al.*, Modeling energy demand for oxygen production on the Moon. Space_resources_LEIA, github repository. github.com/dlite-x/Space_resources_LEIA. Accessed 15 June 2024.
75. R. P. Mueller *et al.*, Design of an excavation robot: Regolith Advanced Surface Systems Operations Robot (RASSOR). *Earth Space* **2**, 163–174 (2017), 10.1061/9780784479971.018.
76. V. I. Balovnev, *New Methods for Calculating Resistance to Cutting of Soil* (U.S. Department of Agriculture, and the National Science Foundation by Amerind Pub. Co., Washington, D.C., 1983).
77. A. Wilkinson, A. DeGennaro, Digging and pushing lunar regolith: Classical soil mechanics and the forces needed for excavation and traction. *J. Terramechanics* **44**, 133–152 (2007).
78. R. He *et al.*, Review of terramechanics models and their applicability to real-time applications. *J. Terramechanics* **81**, 3–22 (2019).

79. W. N. Agosto, Electrostatic concentration of lunar soil minerals. *Lunar Bases Space Act 21st Century* (1985).
80. J. W. Quinn, J. G. Captain, K. Weis, E. Santiago-Maldonado, S. Trigwell, Evaluation of tribocharged electrostatic beneficiation of lunar simulant in lunar gravity. *J. Aerosp. Eng.* **26**, 37–42 (2013).
81. R. R. Oder, Magnetic separation of lunar soils. *IEEE Trans. Magn.* **27**, 5367–5370 (1991).
82. U. Hegde, R. Balasubramaniam, S. Gokoglu, Analysis of thermal and reaction times for hydrogen reduction of lunar regolith. *AIP Conf. Proc.* **969**, 195–202 (2008).
83. P. Hager, D. Binns, "Thermal design challenges for lunar ISRU payloads" in *The 50th International Conference on Environmental Systems* (ICES-2021-180, 2021). ttu-ir.tdl.org/items/e4e57dd5-3a86-45da-90b1-31223e93c59e. Accessed 15 January 2023.
84. S. Schreiner, J. Dominguez, L. Sibille, J. Hoffman, Thermophysical property models for lunar regolith. *Adv. Space Res.* **57**, 1209–1222 (2015).
85. L. M. Anovitz *et al.*, The heat-capacity of ilmenite and phase equilibria in the system Fe-T-O. *Geochim. Cosmochim. Acta* **49**, 2027–2040 (1985).
86. V. Gumen, A. ul Haq, B. Ilyas, A. Maqsood, High-temperature thermal conductivity of ceramic fibers. *J. Mater. Eng. Perform.* **10**, 475–478 (2001).
87. K. Daryabeigi, S. D. Miller, G. R. Cunnington, "Heat transfer in high-temperature multilayer insulation" in *5th European Workshop on Thermal Protection Systems and Hot Structures* (Document ID 20080013560, 2006). ntrs.nasa.gov/citations/20080013560. Accessed 15 January 2023.
88. HyLYZER 400/500 PEM Water Electrolyzers spec sheet. Cummins. mart.cummins.com/imagelibrary/data/assetfiles/0070330.pdf. Accessed 15 January 2023.
89. K. Mazloomi, C. Gomes, Hydrogen as an energy carrier: Prospects and challenges. *Renew. Sustain. Energy Rev.* **16**, 3024–3033 (2012).
90. M. V. Zagarola, J. A. McCormick, High-capacity turbo-Brayton cryocoolers for space applications. *Cryogenics* **46**, 169–175 (2006).
91. H. J. M. ter Brake, G. F. M. Wiegerinck, Low-power cryocooler survey. *Cryogenics* **42**, 705–718 (2002).
92. R. Radebaugh, R. G. Ross, Cryocooler fundamentals and space applications. Information Sources (Jefferson Lab, US Department of Energy, 2015), p. 252. www.jlab.org/IR/Cryocooler_Fundamentals_Course_Notes/CSA-CEC2015.pdf. Accessed 15 January 2023.
93. Active Thermal Control System (ATCS) Overview. www.nasa.gov/wp-content/uploads/2021/02/473486main_iss_atcs_overview.pdf. Accessed 15 January 2023.
94. F. Ghaffari-Tabrizi, J. Haemisch, D. Lindner, Reducing hydrogen boil-off losses during fuelling by pre-cooling cryogenic tank. *Hydrogen* **3**, 255–269 (2022).
95. W. U. Notardonato *et al.*, Zero boil-off methods for large-scale liquid hydrogen tanks using integrated refrigeration and storage. *IOP Conf. Ser. Mater. Sci. Eng.* **278**, 012012. (2017).
96. J. Joseph, G. Agrawal, D. K. Agarwal, J. C. Pisharady, S. Sunil Kumar, Effect of insulation thickness on pressure evolution and thermal stratification in a cryogenic tank. *Appl. Therm. Eng.* **111**, 1629–1639 (2017).
97. External Tank Thermal Protection System, NASA Facts (2005). www.nasa.gov/wp-content/uploads/2016/08/114022main_tps_fs.pdf. Accessed 15 January 2023.
98. H. Simmler *et al.*, Vacuum Insulation Panels – Study on VIP-components and panels for service life prediction of VIP in building applications (Subtask A) (2005). www.osti.gov/etdeweb/biblio/21131463. Accessed 15 January 2023.